IEEE Access
Multidisciplinary | Rapid Review | Open Access Journal

Received April 12, 2021, accepted May 11, 2021, date of publication May 17, 2021, date of current version May 24, 2021.

Digital Object Identifier 10.1109/ACCESS.2021.3081095

Unscrambling for Subgap Density-of-States in Multilayered MoS_2 Field Effect Transistors under DC Bias Stress via Optical Charge-Pumping Capacitance-Voltage Spectroscopy

GA WON YANG [1], SEUNG GI SEO [2], SUNGJU CHOI [1], DAE HWAN KIM [1], (Senior Member, IEEE), AND SUNG HUN JIN [2]

[1]School of Electrical Engineering, Kookmin University, Seoul 02703, South Korea
[2]Department of Electronic Engineering, Incheon National University, Incheon 22012, South Korea

Corresponding authors: Dae Hwan Kim (drlife@kookmin.ac.kr) and Sung Hun Jin (shjin@inu.ac.kr)

This work was supported in part by the Priority Research Centers Program through the National Research Foundation of Korea (NRF) by the Ministry of Education under Grant NRF-2020R1A6A1A03041954, and in part by the Ministry of Science and Information & Communications Technology (ICT) of Korea (MSIT) under Grant 2016R1A5A1012966 and Grant 2020R1A2B5B01001979.

ABSTRACT Herein, we quantitatively analyze the evolution of the subgap density of states (DOSs) for multilayered molybdenum disulfide (m-MoS_2) field effect transistors (FETs) with bilayered SiN_x/SiO_x gate dielectrics under positive bias stress (PBS) and negative bias stress (NBS) by using optical charge-pumping capacitance-voltage spectroscopy. To decouple external gas ambient effects on device instability, hydrophobic fluoropolymers (cyclized transparent optical polymer; CYTOP) are employed for m-MoS_2 FETs followed by the evaluation of subgap-DOSs in the devices for the respective PBS (or NBS). Through extraction of subgap-DOSs and their deconvolution with an analytical model of acceptor (or donor)-like states, it is shown that the device instability is closely correlated with state transitions of DOSs, corresponding to shallow (or midgap) levels for monosulfur vacancy (V_S) (or disulfur vacancy (V_{S2})). Moreover, after PBS, the initial states of $V_S(0)$ (or $H_{S2}(0)$) transit toward $V_S\,(-1)$ (or $H_{S2}(-1)$) via electron trapping, whereas the transition toward $V_S\,(0)$ and $H_{S2}\,(+1)$ during NBS is assessed from the initial $V_S(-1)$ and $H_{S2}\,(0)$ states. Furthermore, technology computer-aided design (TCAD) simulation based on the extracted DOSs properly replicates the measured I-V characteristics of m-MoS_2 FETs with (and without) CYTOP encapsulation. In this study, subgap-DOS characterization via optical charge pumping and validation of the quantitative evolution of subgap-DOSs suggest that this platform can be potentially beneficial for an in-depth understanding of the origins of device instability for transition metal dichalcogenide (MX_2)-based FETs, where M is a transition metal and X is a chalcogenide.

INDEX TERMS MoS_2, field effect transistor, density of state (DOS), bias stress instability, TCAD simulation.

I. INTRODUCTION

For the ultimate scaling of Si devices below sub 3 nm, direct tunneling leakage through the channel from the source to drain electrode can be problematic, leading to a large increase in standby power consumption [1-2]. Thus, transition metal dichalcogenides (TMDCs) with a sizable energy bandgap beyond graphene have attracted much attention as promising candidates for next-generation semiconductors. This is attributed to versatile properties, such as astonishing electrostatic gate coupling and a high effective mass of electrons, leading to less direct tunneling leakage, no dangling bonds, and genuine optical/chemical properties [3-6]. With regard to the development of next-generation semiconductors, device instability is a mandatory issue to be resolved for practical applications at the circuit and system levels, and therefore, understanding the origins of device instability should be a priority [7-8]. Moreover, the reliability issue for

The associate editor coordinating the review of this manuscript and approving it for publication was Rahul A. Trivedi.

This work is licensed under a Creative Commons Attribution 4.0 License. For more information, see https://creativecommons.org/licenses/by/4.0/

next-generation semiconductors is a key challenge because newly explored materials are not mature enough; therefore, there is much room for improvement in material properties, process compatibility with Si technology, and wafer-scaled scalability, extending toward device- and circuit-level operation. Amongst the varieties of TMDCs, multilayered molybdenum disulfide (m-MoS_2) is a suitable representative TMDC due to its easy exfoliation, relatively stable electrical properties, facile preparation, and abundant form of MoS_2 as natural minerals [9-10], leading to tremendous research activities that encompass various studies: basic transport mechanisms, device and circuit level demonstration toward FinFETs and flat panel displays, gas sensors, and emerging new concept of devices [11-20]. In the recent past, device performance improvement, understanding of genuine transport mechanisms in MoS_2 layers, and their electrical properties have been highly elucidated, and hence, an in-depth knowledge has automatically accumulated [20-23]. However, the improvement in understanding device reliability issues and their clear identification via novel electrical characterization methods are not fully quenched, albeit actively researched in the field of device physics [24-27]. In this sense, identification of the subgap density of states (subgap-DOSs) in TMDCs and their correlation between operating conditions and device reliability are indispensable to the improvement of electrical parameters as well as device reliability in MoS_2 field effect transistors (FETs), which is a prerequisite for reliable operation in real applications. Thus, there have been significant activities to investigate the initial state of material properties via ab initio calculations and density of state characterization via optical charge pumping, Terman methods, and multifrequency C-V characterization [28-30]. However, there have been limited reports on detailed subgap-DOSs and their evolution for the corresponding bias stress for MoS_2 FETs, and moreover, the origin of subgap-DOSs and their variation associated with both external gas ambients (e.g., O_2, H) and internal atomic structure deformation remain elusive even after tremendous research activity in this field [28-37]. This is possibly due to several hurdles: (i) the inability to prepare almost identical device ensembles associated with the absence of a mature, scalable process scheme for the preparation of active layers, (e.g., MoS_2 layers) with both high crystallinity and wafer-scaled substrates, (ii) limited scanning range for trap characterization based on conventional trap characterization methods such as Terman methods for D_{it} [29], multifrequency method for near conduction bands [30], and hysteretic gate transfer characteristics for deep level traps [31]. Thus, full-range characterization for subgap-DOSs is typically prohibited by the method itself and its characterization, leading to limited reports. However, there was a systematic report to characterize the full range of subgap-DOSs for m-MoS_2 FETs by using the optical charge pumping method, which has been popularly utilized and studied for the investigation of the reliability of a-IGZO TFTs with full maturity up to the commercialization level in AMOLED panels [38-43]. Interestingly, entire investigations on device reliability and its evolution on subgap-DOSs, corresponding to positive (or negative) bias stress (PBS or NBS), are completely missing, albeit specifically reported for initial subgap-DOSs for m-MoS_2 FETs with (or without) hydrophobic polymer (e.g., CYTOP) encapsulation [28].

On the other hand, there have been systematic reports on device instability on m-MoS_2 FETs under DC and pulsed mode operation, corresponding to positive and negative bias temperature stresses. Although in-depth studies on device instability for m-MoS_2 FETs were recently reported in the literature [44-45], thermal oxides (SiO_2) on heavily phosphorus-doped Si substrates were used as gate dielectrics for all devices, and therefore, device instability studies on m-MoS_2 FETs with one of the most popular gate dielectrics, for example, PECVD-based dielectrics, SiO_x (or SiN_x) in flat panel display backplanes, have not been explored. Furthermore, all analyses in previous reports have not addressed quantitative trap levels and their trap location in the energy bandgap of m-MoS_2 FETs for the corresponding positive or negative bias stress. Thus, the origin of device instability and quantitative evolution of subgap-DOSs according to the bias stress polarity and its time duration have not been explored for m-MoS_2 FETs with PECVD oxide gate dielectrics.

In the present work, we have investigated quantitative device instability for m-MoS_2 FETs by monitoring the evolution of subgap-DOSs via optical charge pumping, which was reliably well established in a systematic way in terms of quantitative analysis and TCAD-based validation. With a comparison of subgap-DOSs for positive and negative stress for m-MoS_2 FETs either with CYTOP encapsulation or without encapsulation, the contribution toward device instability associated with oxygen or moisture ($\sim OH^-$) and subgap-DOSs are quantitatively analyzed. All origins and their device instability issues associated with subgap-DOSs, identified via the optical charge pumping method, are qualitatively analyzed, and their evolution for each trap and device instability corresponding to subgap-DOSs are thoroughly interpreted in a quantitative mode, in comparison with conventionally accepted origins of device traps to address: (i) the effects of conduction band edge, Mo 4d orbital, (ii) valence band edge via hybridization of Mo 4d orbital and S 3 orbitals, and (iii) midgap states associated with disulfur vacancy, and (iv) shallow trap states correlated with monosulfur vacancy [46-48]. The entire analysis can provide us with insight into the physical origins behind the critical mechanisms that cause device instability behaviors for the respective PBS and NBS observed in this work, among the aforementioned candidates. Moreover, the origins of subgap-DOSs and their correlation between subgap-DOSs and O_2, OH^-, and sulfur vacancies are quantitatively analyzed and discussed. In addition, this study potentially suggests guidelines on how to improve device instability during operation and device implementation with a full understanding of the experimental results and their origins.

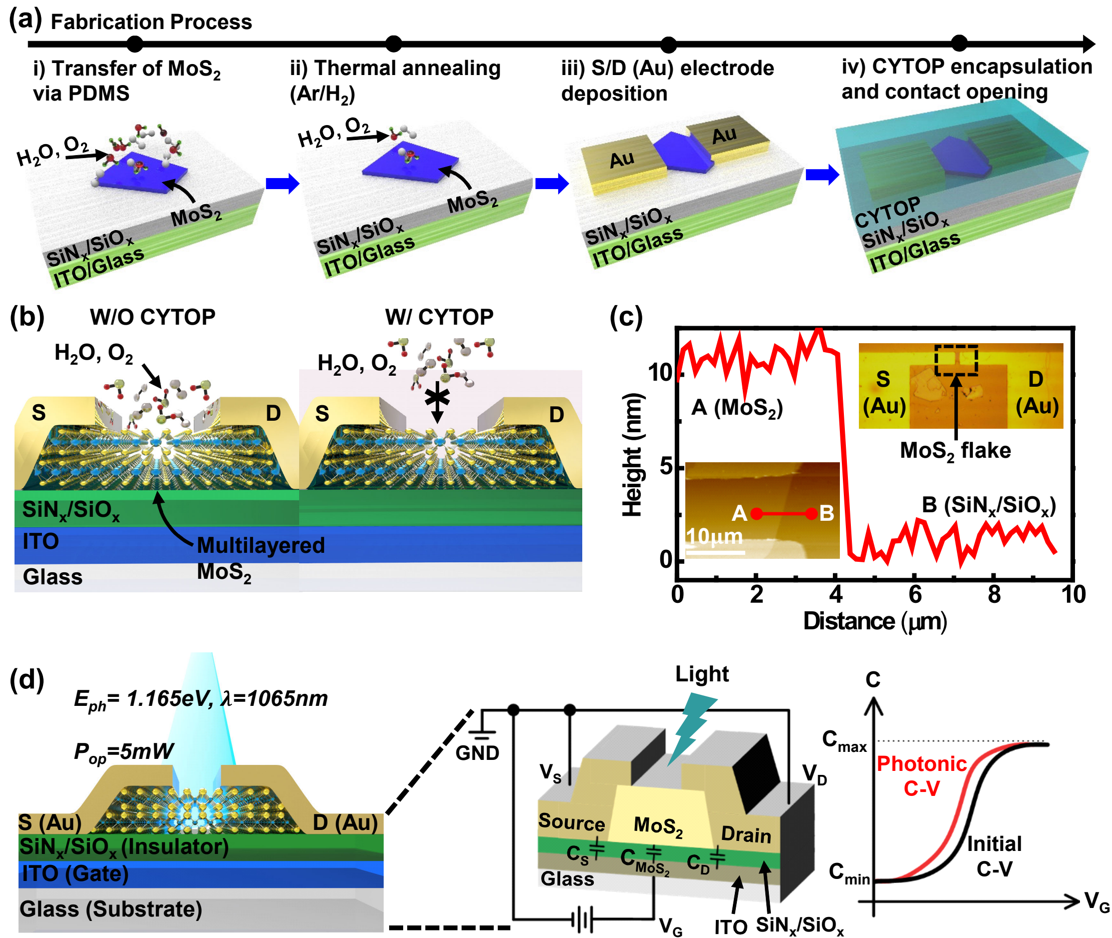

FIGURE 1. (a) Fabrication process of m-MoS_2 FET with CYTOP passivation. (b) The whole device structures with and without CYTOP passivation. (c) Height profile for an m-MoS_2 flake in the channel regime scanned by AFM. Insets show optical microscope images for m-MoS_2 FETs. A and B in the inset denote the location of m-MoS_2 and oxide (SiO_2), respectively. The channel width to length (W/L) is 30/10 μm (d) Conceptual plots for capacitance-voltage measurement captured by optical charge pumping technique.

II. EXPERIMENTAL METHOD

A. FIELD EFFECT TRANSISTOR FABRICATION AND CHARACTERIZATION

Fig. 1(a) shows the process sequence for the fabrication of m-MoS_2 FETs. Indium tin oxide (ITO)-coated glass was used as a starting substrate, playing the role of a gate electrode, followed by ITO etching by dipping in ITO etchant solution to make an island structure. After etching, a gate insulator layer of SiN_x/SiO_2 (200 nm/50 nm) was deposited by plasma-enhanced chemical vapor deposition (PECVD) at the substrate temperature of 350 °C without vacuum breaking, followed by a gate contact opening. Thereafter, multilayers of MoS_2 were mechanically exfoliated from bulk MoS_2 crystals (SPI Supplies, 429 ML-AB) and transferred onto ITO glass substrates using a polydimethylsiloxane (PDMS) elastomer. Immediate annealing was performed in a mixed gas (~Ar/H_2) at 400 °C for 1 hour to remove organic residues from the MoS_2 flakes, which might contaminate them during the transfer process. Thereafter, a 30 nm thick layer of Au was evaporated using thermal evaporators, followed by lifting off on a photolithographically patterned area, forming the source/drain electrodes. The backside of the m-MoS_2 FETs was passivated by amorphous fluorinated polymer (CYTOP; CTL-809 M, Asahi Glass Co., Ltd) using a spin coating process, followed by baking at 150 °C for 1 hour in a glove box with ambient Ar. Thereafter, dry etching (~O_2/CF_4) was performed to make open S/D contact pads for electrical addressing. The front view of the fabricated device is displayed in Fig. 1(b). Thereafter, atomic force microscopy (AFM), as shown in Fig. 1(c), confirmed that the thickness of the m-MoS_2 was 10 nm, which is equivalently extracted as 15 layers of MoS_2. All electrical characterizations were measured with a semiconductor parameter analyzer (Agilent 4284A) in ambient air at room temperature. Transfer characteristics were obtained at V_{DS} = 0.1 V. The thickness of the MoS_2 flakes was measured by atomic force microscopy (AFM, Park system, XE-100).

B. OPTICAL CHARGE-PUMPING CAPACITANCE-VOLTAGE SPECTROSCOPY

In this study, for the extraction of subgap-DOSs in m-MoS_2 FETs, we utilized well-established optical charge-pumping capacitance-voltage (C-V) spectroscopy [38-39, 49]. The technique, as shown in Fig. 1(d), basically uses monochromatic photonic capacitance-voltage (MPCV) characterization. The capacitance between the bottom gate and S/D electrodes for m-MoS_2 FETs was evaluated in the dark and under light illumination with a laser wavelength (λ) of 1065 nm. C-V characteristics were measured by an HP4284A precision LCR meter at a frequency of 10 kHz under dark and light illumination with a wavelength of λ = 1065 nm to extract the full range of trap information in subband gaps. For the identification of subgap-DOSs for multilayered MoS_2, a laser source with a wavelength of 1065 nm, which has an energy of $E_{ph} = 1.24/\lambda_o = 1.165$ eV, was used. In the present work, a wavelength of 1065 nm was intentionally selected in consideration of the energy bandgap of m-MoS_2 layers because lasers with wavelengths shorter than 1065 nm have a higher chance of exciting electrons located in the valence band toward conduction via band-to-band generation, leading to overestimation of the density of trapped charges. Moreover, optical power was selected in this work at a condition of 5 mW after confirming the saturation behaviors on photoresponse, which is similar to the method reported in the literature [28]. As shown in Fig. 1(d) middle, the minimum capacitance (C_{min}) is determined by the total overlapping area between the source and drain electrodes (C_S and C_D) and the gate electrodes. In addition, a conceptual capacitance-voltage plot, as shown in Fig. 1(d) on the right, shows that the capacitance difference (C_{max}-C_{min}) between the maximum capacitance (C_{max}) and minimum capacitance (C_{min}) yields the capacitance for the active region of MoS_2 layers (C_{MoS2}), which can be modulated by gate-to-source voltage (V_{GS}). These capacitance values can be differentiated before and after light illumination, yielding a difference in charge carriers in the MoS_2 channel due to optically pumped charge carriers from the inside bandgap of MoS_2 under light illumination. With this method, the photonic C-V and subgap-DOSs of m-MoS_2 FETs before and after bias stress can be measured, from which their correlation between subgap-DOSs and bias stress instability was investigated.

C. TCAD VALIDATION

TCAD simulations were performed by incorporating the band structure, subgap density of the state model, advance mobility, and tunneling model into SILVACO ATLAS-2D. The band structure was simplified to several quantities: the energies of the conduction and valence band edges and the density-of-states masses for electrons and holes of each material. The trap-limited transport model was activated in this simulation. Additionally, an advanced mobility model including phonon scattering, Coulomb scattering, surface roughness, and subgap density of state effects was applied.

III. RESULTS AND DISCUSSION

A. BIAS STRESS INSTABILITY OF m-MoS_2 FETs

For the evaluation of external gas ambient effects on the performance of m-MoS_2 FETs, CYTOP encapsulation was employed, and the initial electrical characteristics before encapsulation of CYTOP were evaluated with the same protocols reported in the literature [37]. For a fair comparative study, all electrical characteristics without and with CYTOP encapsulation were evaluated, and a systematic comparison was performed. Fig. 2(a) and its inset show transfer characteristics for m-MoS_2 FETs with and without CYTOP on a log scale and linear scale, respectively. Owing to outstanding encapsulation effects reported in the literature [37, 45, 50], suppression of external ambient gas effects (i.e., H_2O and O_2) on the back channel region of MoS_2 flakes leads to noticeable improvement of electrical properties on subthreshold swing (S.S) and field effect mobility (μ_{FE}). As external ambient gases were identified to cause additional trap sites in MoS_2 layers [34-37], encapsulation effects were shown to be closely related to instability issues. Figs. 2(b) and (c) show that a net threshold voltage shift (ΔV_{th}) is 2.3 V (or 1.9 V) for m-MoS_2 FETs without (or with) CYTOP under positive gate bias stress of 5 V, respectively, where V_{th} is extracted using constant current at $I_{DS} = 10^{-8}$ A. Moreover, Figs. 2(d) and (e) show that the respective V_{th} shift is extracted as −2.6 V (or −1.9 V) for m-MoS_2 FETs without (or with) CYTOP encapsulation under a negative gate bias stress of −5 V. The stress voltage was applied for approximately an hour considering the overdrive voltage. The reduced V_{th} shift value after CYTOP encapsulation substantiates the decrease in the total number of trap sites, which might originate from the back channel interface and defects inside the MoS_2 layers. Fig. 2(f) illustrates the bandgap models for charge trapping under bias stress conditions. Under PBS (or NBS), electrons (or holes) can be trapped in both insulator and subgap-DOSs of m-MoS_2. In particular, a larger V_{th} shift under negative bias stress for m-MoS_2 FETs with thermal gate oxide (SiO_2) was frequently reported, which is attributed to the large population of hole traps, possibly coming from sulfur vacancies of MoS_2, as observed in the previous literature [44-45]. However, the origin on different levels of ΔV_{th} for the respective NBS (or PBS) may be attributed to the combination effects that result from gate dielectrics, their interface between an active layer and a gate dielectric, and the active layer itself. Hence, in this study, after CYTOP encapsulation, the absolute value of ΔV_{th} for NBS is slightly larger than (or similar to) that of ΔV_{th} for positive conditions, which is possibly due to synergetic effects coming from PECVD-based gate dielectrics and O_2 and H_2O molecules.

With respect to the overall trend of electrical properties, Figs. 3(a), (b) and (c) show the detailed electrical properties, where S.S and μ_{FE} are extracted from $S.S = \{(\partial \log I_{DS}/\partial V_{GS})_{max}\}^{-1}$ and $\mu_{FE} = L \cdot g_m (W C_i V_{DS})^{-1}$. In addition to the reduction of ΔV_{th}, the standard deviation for ΔV_{th} and $\Delta\mu_{FE}$ is also remarkably reduced after CYTOP encapsulation, which enables us to secure uniform and

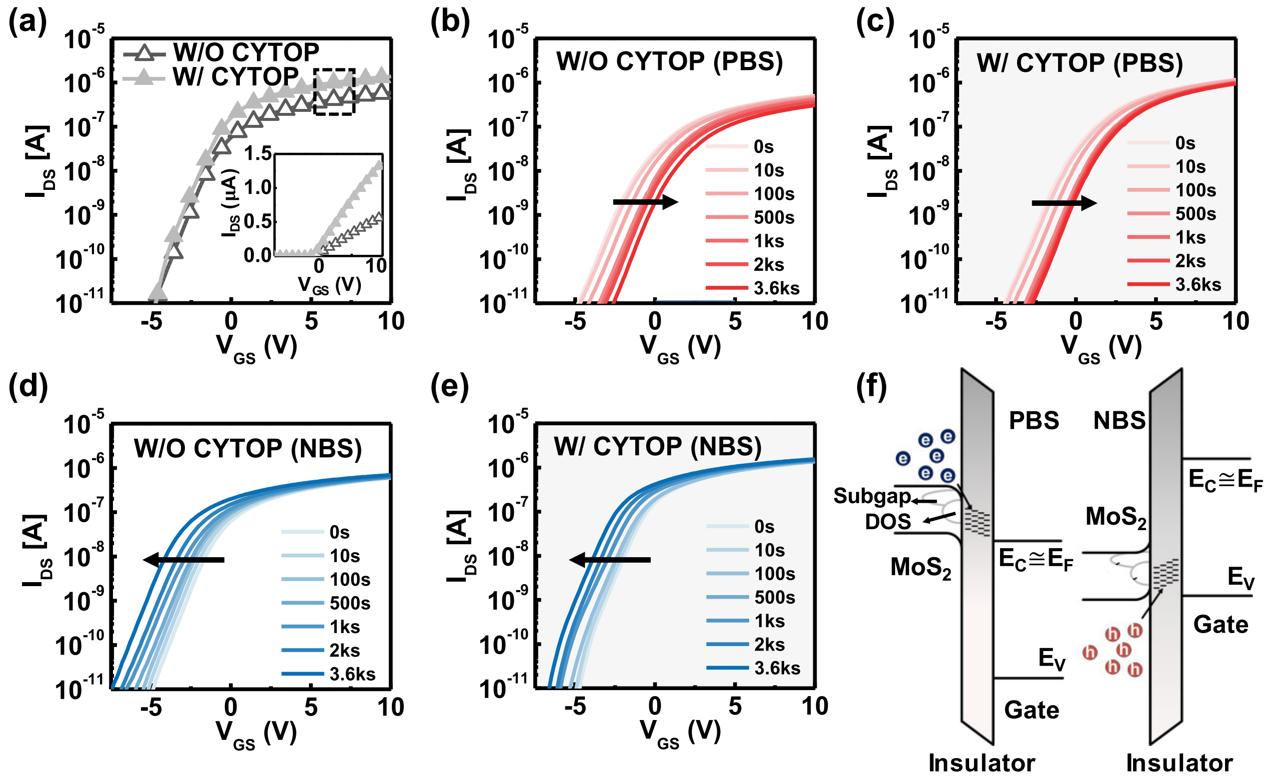

FIGURE 2. (a) Comparison on initial transfer characteristics of m-MoS_2 FET without and with CYTOP encapsulation at V_{DS} =0.1 V in log scale. Insets in Fig. 2(a) shows initial transfer characteristics of m-MoS_2 FET without and with CYTOP encapsulation at V_{DS} =0.1 V in linear scale. (b) Transfer characteristics of m-MoS_2 FET without CYTOP encapsulation after PBS at V_{DS} =0.1 V in log scale. (c) Transfer characteristics of m-MoS_2 FET with CYTOP encapsulation after PBS at V_{DS} =0.1 V in log scale. (d) Transfer characteristics of m-MoS_2 FET without CYTOP encapsulation after NBS and (e) transfer characteristics of m-MoS_2 FET with CYTOP encapsulation after NBS at V_{DS} =0.1 V in log scale. (f) Energy band diagrams to describe the charge trapping mechanisms of the m-MoS_2 FETs under PBS and NBS.

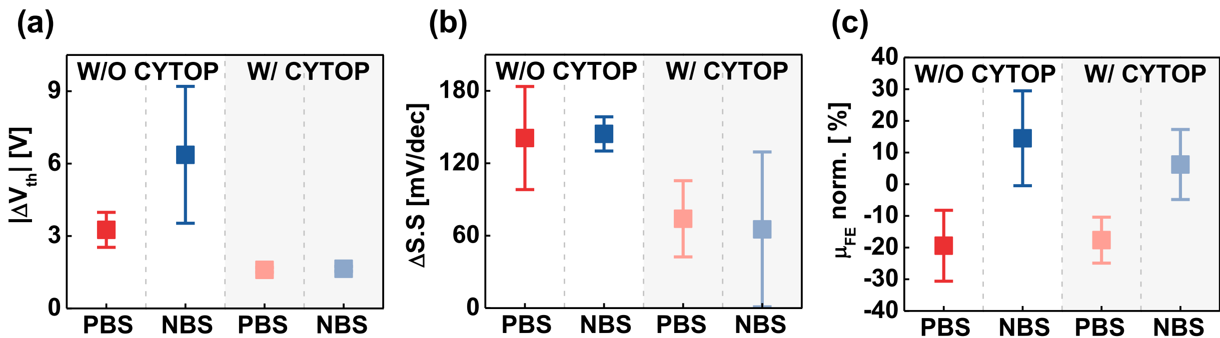

FIGURE 3. (a) ΔV_{th} in m-MoS_2 FET without and with CYTOP encapsulation after PBS and NBS. (b) ΔS.S in m-MoS_2 FET without and with CYTOP encapsulation after PBS and NBS. (c) Normalized mobility in m-MoS_2 FET without and with CYTOP encapsulation after PBS and NBS.

improved stability properties of m-MoS_2 FETs regardless of device variation. On the other hand, bias stress effects on electrical properties, corresponding to a bias polarity during bias stress, were differently observed, according to the device encapsulation. Regardless of CYTOP encapsulation, the values of S.S increase for both PBS and NBS, whereas μ_{FE} decreases (or increases) for PBS (or NBS). This behavior is possibly attributed to the change in trap densities and their distribution during device operation. However, if the apparently observed results stand alone, it could be highly uncertain to reach a reliable and detailed analysis on device instability because trap distribution and its variation are relatively hard to analyze by bias stress instability data and their instability model standalone. In this regard, MPCV spectroscopy was adopted to investigate the fundamental origins of device instability, variation in electrical properties, and their correlation with subgap-DOSs of m-MoS_2, which can evolve on a time scale during bias stress tests.

B. EXTRACTION OF SUBGAP-DOSs FOR m-MoS_2 FETs

Experimental platforms for optical charge pumping capacitance-voltage spectroscopy and their extraction

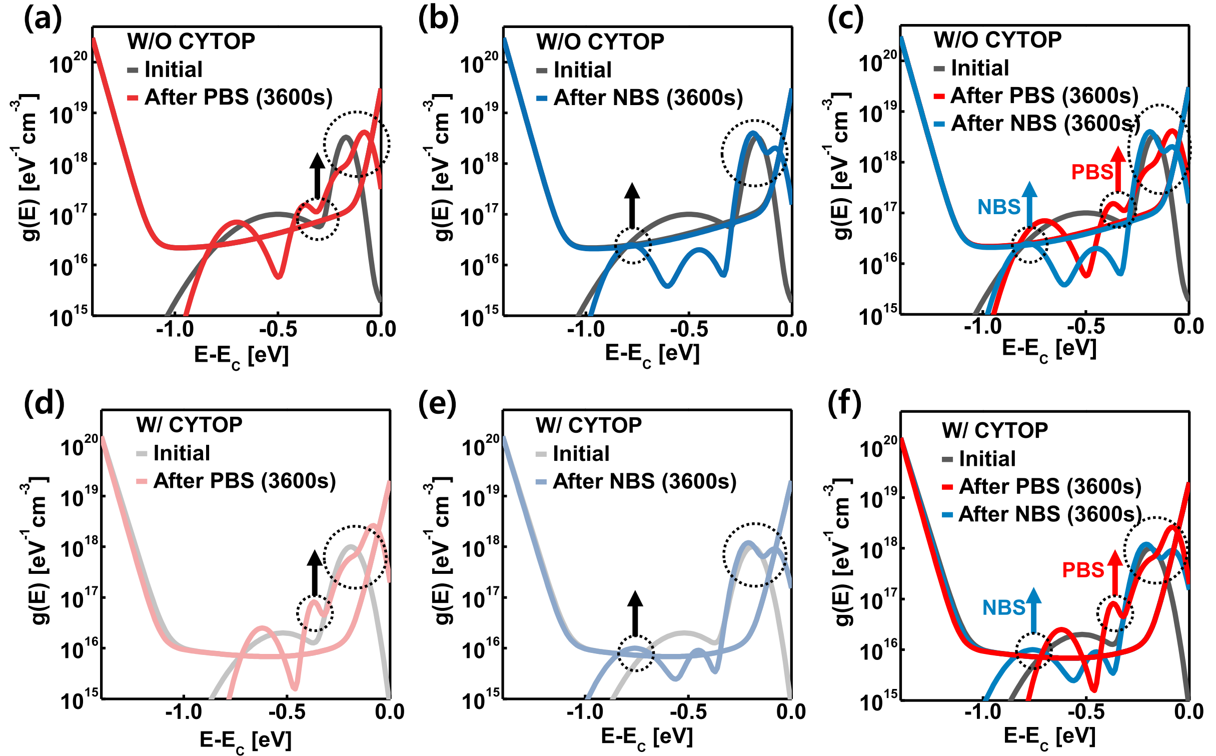

FIGURE 4. Deconvoluted DOSs from the m-MoS_2 FET without CYTOP encapsulation (a) before and after PBS, (b) before and after NBS, and (c) overlapped data of Fig. 4(a) and (b). Deconvoluted DOSs from the m-MoS_2 FET with CYTOP encapsulation (d) before and after PBS, (e) before and after NBS, and (f) overlapped data of Fig. 4(d) and (e).

procedures were reported in the literature [38-39]. Based on the measured photonic C-V characteristics and their standard procedures for the extraction of subgap-DOSs reported in the literature, subgap-DOSs for m-MoS_2 FETs, as shown in Fig. 4, were extracted and plotted, corresponding to positive (or negative) bias stress for m-MoS_2 FETs without (or with) CYTOP encapsulation. Acceptor-like states (g_A) and donor-like states (g_D), according to Equations (1) and (2), are analytically modeled and deconvoluted, yielding information on subgap-DOSs.

$$g_A(E) = g_{TA}(E) + g_{DA}(E) = N_{TA} \exp\left(-\frac{E_C - E}{kT_{TA}}\right) + N_{DA} \exp\left(-\frac{E_C - E}{kT_{DA}}\right) \quad (1)$$

$$\begin{aligned} g_D(E) &= g_{TD}(E) + g_{DD}(E) + g_{SD}(E) + g_{Mid}(E) \\ &= N_{TD} \exp\left(-\frac{E - E_V}{kT_{TD}}\right) + N_{DD} \exp\left(-\frac{E - E_V}{kT_{DD}}\right) \\ &\quad + + N_{SD} \exp\left\{-\left(\frac{E_C - E_{SD} - E}{kT_{SD}}\right)^2\right\} \\ &\quad + N_{Mid} \exp\left\{-\left(\frac{E - E_V - E_{Mid}}{kT_{Mid}}\right)^2\right\} \end{aligned} \quad (2)$$

where g_{TA} (E) is for acceptor-like tail states, g_{DA} (E) for acceptor-like deep states, g_{TD} (E) for donor-like tail states, g_{DD} (E) for donor-like deep states, g_{SD} (E) for shallow-donor states, and g_{Mid} (E) for mid gap defect states, depending on the type of energy level distribution. In addition, the characteristic energy distribution and Gaussian center of energy are defined as kT_{DOS} (e.g., T_{TA}, T_{DA}, T_{TD}, T_{DD}, $T_{SD,}$ and T_{Mid}) and E_{DOS} (e.g., E_{SD}, E_{Mid}), respectively, and are extracted. Herein, N_{DOS} (e.g., N_{TA}, N_{DA}, N_{TD}, N_{DD}, N_{SD}, and N_{Mid}) represents each energy density distribution of traps, E_V represents the valance band maximum, and E_C represents the conduction band minimum, which are magnificently fitted with the model parameters represented by Equations (1) and (2). All extracted subgap-DOSs are fitted with the analytical models for Equations (1) and (2), leading to smooth functions for subgap-DOSs, as shown in Fig. 4. Subgap-DOSs are deconvoluted using conventional trap states such as acceptor-like states (e.g., Eq. (1)) and donor-like states (e.g., Eq. (2)), respectively, yielding information for a quantitative understanding. In particular, it is generally reported that the μ_{FE} in n-channel FETs is significantly affected by defects near E_C [28]. Several key parameters, such as g_{TA} (E), g_{SD} (E), and g_{DA} (E), below E_c are energetically distributed throughout the energy bandgap with energy location dependency, yielding capture and thermal release of free carriers in certain energy states, such as multiple trapping and thermal release events [28]. Fig. 5 shows schematic cartoons to illustrate the reduction of frequency in multiple trapping and release due to CYTOP passivation, which has the effects of prohibition of external gas adsorption toward sulfur vacancy,

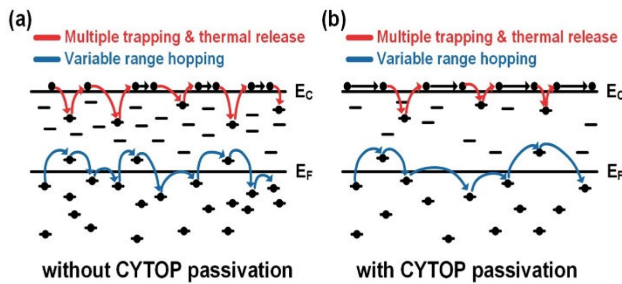

FIGURE 5. Schematic cartoons to illustrate variable range hoping and multiple trapping and thermal release behaviors in m-MoS_2 FETs (a) with and (b) without CYTOP passivation.

possibly located in defects in active layer of MoS_2 and interface between MoS_2 and gate dielectric. As per Fig. 5, the bias condition is the same condition corresponding to the same gate-overdrive voltage.In this sense, capture probability should be reduced when trap levels in forbidden bandgaps are reduced due to passivation. More importantly, field effect mobility improvement after passivation can be determined not by "trap level reduction itself" but by "how much reduction of trap levels", which are located in the energy level around E_F at certain temperature and applied bias condition.

To better understand the characteristics of subgap-DOSs for m-MoS_2 FETs under bias stress, we extracted and analyzed detailed subgap-DOSs for m-MoS_2 FETs after the respective PBS (or NBS) for 1 hour. Fig. 4(a) (or (b)) shows deconvoluted curves for subgap-DOSs, g(E), which are fitted with experimentally extracted DOSs for m-MoS_2 FETs without CYTOP encapsulation after positive (or negative) bias stress. For a better comparison, two data points are plotted in overlapping mode, which is displayed in Fig. 4(c). On the other hand, Fig. 4(d) (or (e)) shows deconvoluted curves for subgap-DOSs and g(E) for m-MoS_2 FETs with CYTOP encapsulation after positive (or negative) bias stress. For a clear and intuitive comparison, two data points overlap in the same graph, which is displayed in Fig. 4(f). After PBS for 1 hour, Fig. 4(a) (or (d)) illustrates that some values in the N_{SD} (or N_{Mid}) peaks, which are located closer to E_C (or further away from E_V), respectively, were increased for m-MoS_2 FETs regardless of CYTOP encapsulation. On the other hand, after NBS for 1 hour, Fig. 4(b) (or Fig. 4(e)) shows that some values in the N_{SD} (or N_{Mid}) peaks, which are located further away from E_C (or closer to E_V), increased for m-MoS_2 FETs regardless of CYTOP encapsulation. Overall, a noticeable change in DOSs was observed after PBS (or NBS), hinting that subgap states for m-MoS_2 were discernably changed, followed by redistribution of subgap states in the allowed DOSs. Thereafter, systematic modeling and extraction procedures are applied to subgap-DOS parameters, yielding quantitative values, as displayed in Fig. 4.

From the extracted and fitted DOS results, the atomic structure and DOSs model of MoS_2 are shown in Fig. 6. Figs. 6(a), (b), and (c) illustrate the atomic configuration in a MoS_2 layer for the respective views of top, side, and 3D, corresponding to a pristine monosulfur vacancy (V_S) and a disulfur vacancy (V_{S2}) in m-MoS_2. Fig. 6(d) indicates the DOSs model extracted from our m-MoS_2 FETs. As revealed in the literature [46-48, 51], the origin for each state could be conceived, accordingly, for the respective of (i) conduction band edge for Mo 4d orbital, (ii) valence band edge for hybridization of Mo 4d orbital and S 3p orbitals, (iii) midgaps for disulfur vacancy (V_{S2}), and (iv) possible shallow trap states for monosulfur vacancy (V_S).

In the subgap DOSs of MoS_2, V_S and V_{S2} are dominant owing to their low formation energy [48]. However, other representative defects, such as molybdenum vacancies, were excluded owing to their very high formation energy [48, 52]. Figs. 6(e) and (f) indicate DOSs models after 1 hour of PBS and NBS, respectively [48, 52-54]. In particular, for the case of a disulfur vacancy, combination with hydrogen might occur, leading to transformation toward a hydrogenated disulfur vacancy (H_{S2}) [52]. During PBS, a shift of the Fermi energy level (E_F) upwards results in the occupation of electrons onto the V_S state, which can be attributed to the transition toward V_S (-1) via the adoption of electrons, and moreover, H_{S2} can be changed into the H_{S2} state (-1) due to the attraction of electrons. When the state transition for V_S and H_{S2} predominantly occurred, the increase in states, according to the (-1) state peak of V_S and H_{S2}, should be rationally expected. On the other hand, during NBS, the Fermi energy level (E_F) moves downwards, and V_S (-1) can transition into the state of V_S (0) by combining with positive holes. In addition, H_{S2} can be changed into the state of $H_{S2}(+1)$ by combining with positive holes. Thus, when a predominant transition can occur, the leading state change from V_S (-1) (or H_{S2}) to $V_S(0)$ ($H_{S2}(+1)$), and the increase in peak states for $V_S(0)$ (or $H_{S2}(+1)$) are rationally predicted after NBS stress.

For a quantitative comparison, detailed DOSs for all peaks and their energy location, corresponding to usage of encapsulation and bias stress condition, were compared in Fig. 7. Regardless of CYTOP encapsulation, Figs. 7(a), (b) show that the N_{TA}, N_{DA}, N_{DD}, and N_{TD} peaks remain in their original state even after PBS and NBS. However, compared to the information on DOSs for m-MoS_2 FETs without CYTOP, % reduction for the respective trap state after CYTOP encapsulation is estimated to be 33% for N_{TA}, 93% for N_{DA}, 50% for N_{TD}, and 40% for N_{DD}, which is consistent with the results of ΔV_{th} reduction with CYTOP encapsulation in Fig. 3(a).

All results and their trends on the evolution for subgap-DOSs after CYTOP encapsulation are on the same page as previously reported data in the literature [28]. On the other hand, as mentioned before, Figs. 7(c) and (d) display that $V_S(-1)$ (or $H_{S2}(-1)$) peaks after PBS were increased to the value of 4×10^{18} (or 1.5×10^{17}) for the device without CYTOP and 1.5×10^{18}(or 1×10^{17}) for the device with CYTOP, respectively, as compared to the value of 8×10^{17} (W/O CYTOP) and 6×10^{17}(W/CYTOP) for $V_S(0)$ and the value of 7×10^{16}(W/O CYTOP) and 2.5×10^{16}(W/CYTOP)

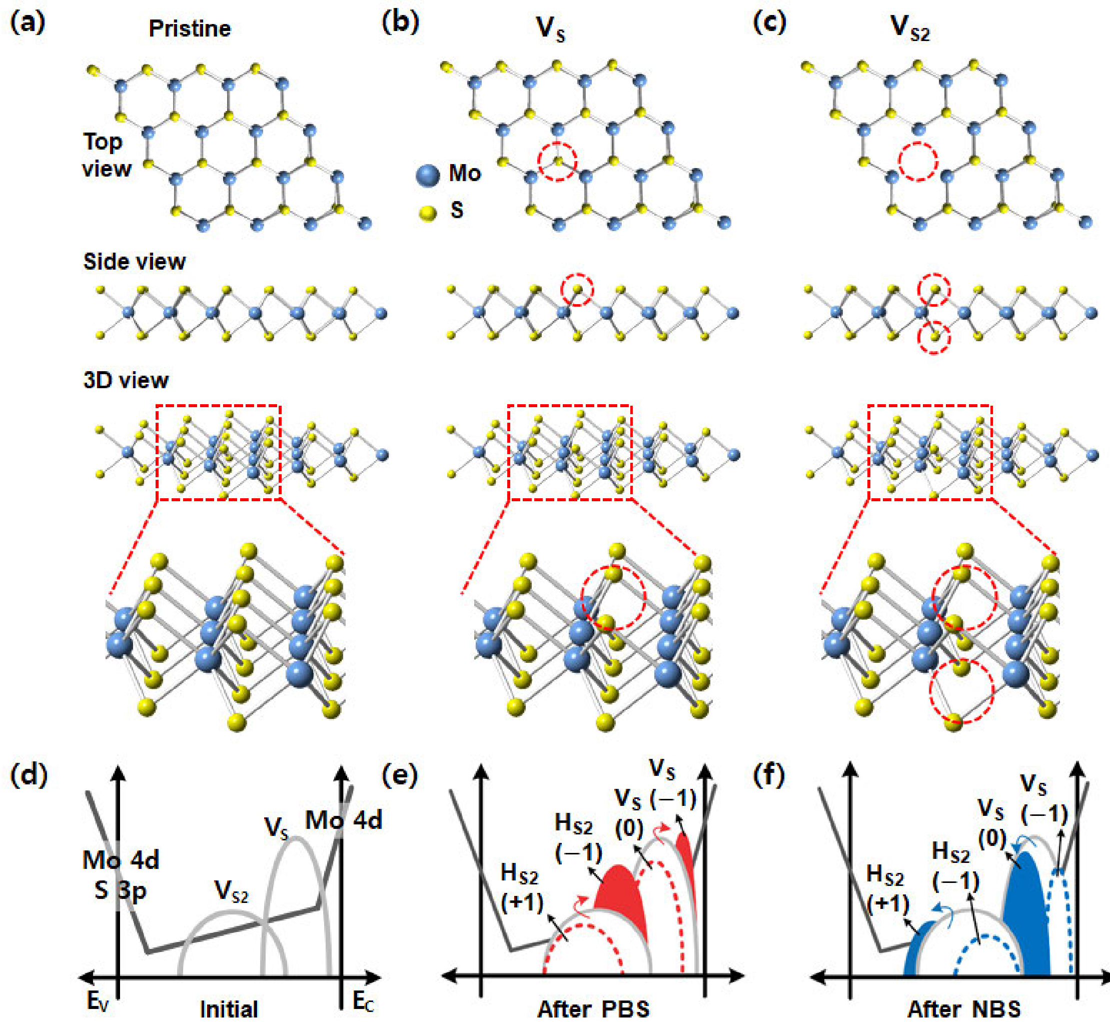

FIGURE 6. Atomic structure for (a) pristine. (b) Monosulfur vacancy (V_S). (c) Disulfur vacancy (V_{S2}). Schematic cartoon about (d) initial DOSs model and DOSs model after (e) PBS and (f) NBS in m-MoS_2 FET.

for H_{S2} (+1), accordingly. In addition, $V_S(0)$ (or $H_{S2}(+1)$) peaks after NBS show higher values of 4×10^{18} (or 2.5×10^{16}) for the device without CYTOP and 1.2×10^{18} (or 1×10^{16}) for the device with CYTOP compared to the values of 2×10^{18}(W/O CYTOP) and 9×10^{17} (W/CYTOP) for $V_S(-1)$ and 2×10^{16} (W/O CYTOP) and 9×10^{15} (W/CYTOP) for H_{S2} (−1), respectively.

For further confirmation of the peak transition of V_S and V_{S2} after bias stress, the energy location of each peak was extracted. Fig. 7(e) shows that the N_{Mid} peak with the highest value for the bare device W/O CYTOP was changed from the initial value of 0.50 eV to 0.37 eV (or 0.78 eV) after PBS (or NBS). On the other hand, the N_{SD} peak with the highest value for the bare device was changed from the initial value of 0.17 eV to 0.05 eV (or 0.19 eV) after PBS (or NBS), accordingly. Due to the transition of V_S and V_{S2} toward a negative state after PBS (or a positive state after NBS), the energy locations of the N_{Mid} and N_{SD} peaks, which are closely associated with V_S and V_{S2}, are shifted to near E_C (or toward E_V). Likewise, for the W/CYTOP device, Fig. 7(f) shows that the N_{Mid} peak with the highest value was changed from the initial value of 0.52 eV to 0.37 eV (or 0.76 eV) after PBS (or NBS). Moreover, the N_{SD} peak with the highest value moved from the initial value of 0.19 eV to 0.08 eV (or 0.21 eV) after PBS (or NBS), respectively.

All results, as shown in Fig. 7, substantiate that the effects of bias stress for m-MoS_2 FETs are closely correlated with subgap states and that their information on the evolution of DOSs is beneficial to understand the quantitative contribution toward electrical parameters, including V_{th} and S.S, and μ_{FE}, and others. Furthermore, these results are reasonably matched with the variation in electrical properties for m-MoS_2 FETs after bias stress. Similar to the evolution of electrical parameters in Fig. 3, S.S increases and μ_{FE} decreases after PBS, and S.S and μ_{FE} increase after NBS, respectively. The degradation on S.S after PBS (or NBS) might be attributed to the widened N_{SD} peak after bias stress. Moreover, the decreased μ_{FE} after PBS can originate from an increase in impurity

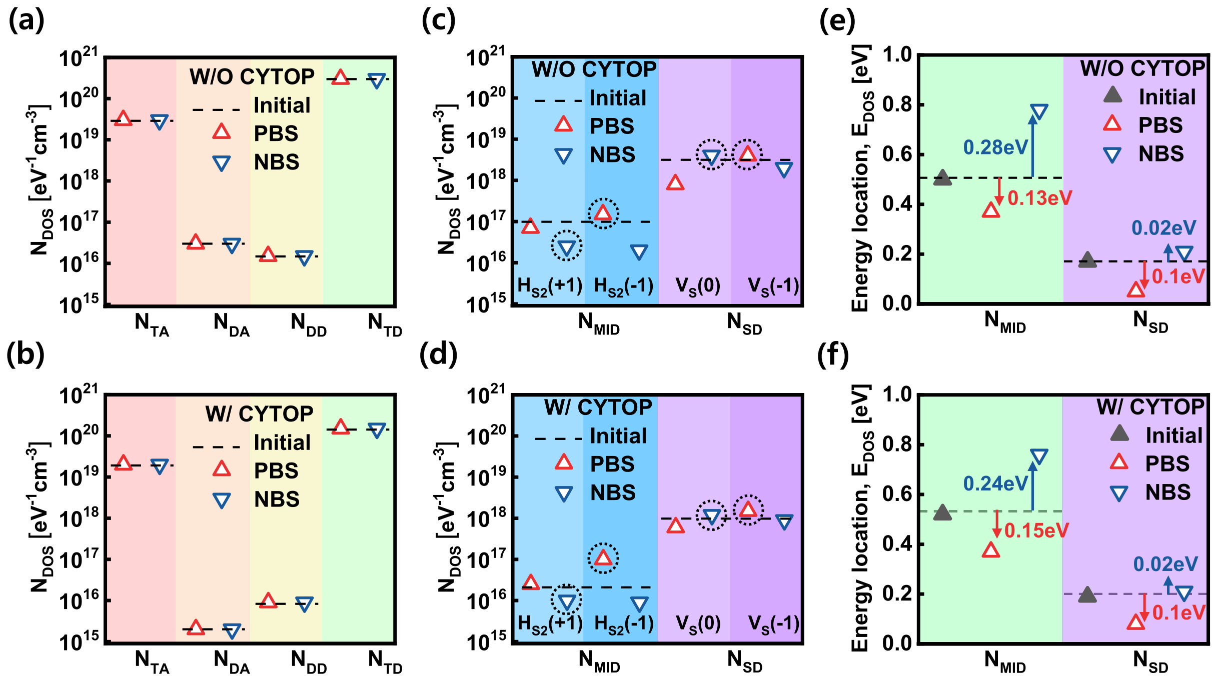

FIGURE 7. Comparison on N_{TA}, N_{DA}, N_{DD}, N_{TD}, N_{MID}, N_{SD} states level and their energy locations of m-MoS_2 FET (a), (c), (e) without and (b), (d), (f) with CYTOP encapsulation after PBS and NBS.

scattering, possibly due to the generation of $V_S(-1)$ states during PBS. On the other hand, the variation in the evolution of μ_{FE} according to the stress time of NBS was relatively small compared to that of PBS. This is within a similar trend of μ_{FE} evolution for m-MoS_2 FETs for PBS (or NBS) in the literature [44,45]. For quantitative visualization and its easy understanding of the trend of evolution for DOSs, all the information on the extracted DOSs is summarized in Table 1 (W/O CYTOP) and Table 2 (W/CYTOP), respectively. In the present work, with an adoption of the values in Tables 1 and 2, the information of DOSs before (or after) bias stress for m-MoS_2 FETs with (or without) CYTOP encapsulation is displayed in Fig. 7 for a clear delivery of the trend of evolution of DOSs.

C. TCAD SIMULATION

To validate the physical meaning of the extracted subgap-DOSs from the perspective of device operation, a technology computer-aided design (TCAD) simulation was performed using Atlas 2-D of SILVACO [55-57]. TCAD simulation was performed by changing Si-based model parameters and electrical parameters because multilayer MoS_2 is typically known to have an indirect bandgap. Thus, transfer characteristics for m-MoS_2 FETs via TCAD simulation were obtained from experimentally extracted DOSs, g(E), by using optical charge pumping C-V spectroscopy. As shown in Fig. 8, we simulated I-V data with structural parameters and material parameters. Additionally, we enhanced the accuracy of the simulation by comparing the electrical parameters of the measured I-V data with the

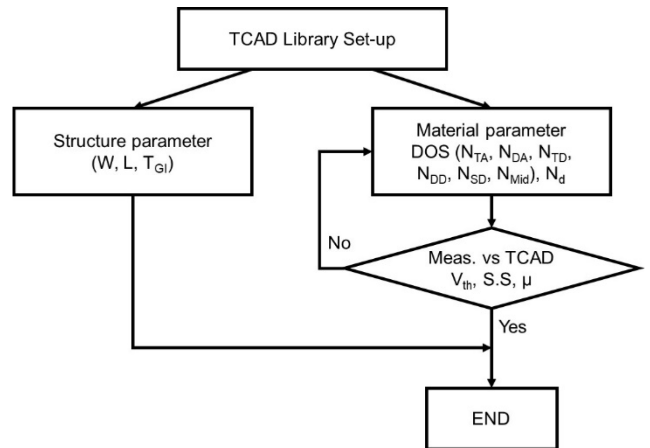

FIGURE 8. Flow diagram for the TCAD simulation.

electrical parameters of the simulated I-V data. Fig. 9 shows changes in electrical properties according to DOS parameters. As a result, it is confirmed through simulation that DOSs near the conduction band have a significant impact on electrical parameters. In particular, because the DOS parameter N_{Mid} and N_{SD} reduction can contribute to the increase in mobility and current level in transfer curves, we fitted the mobility by using these values, leading to extraction of field effect mobility. In addition, doping concentration (N_d) reduction can contribute to a decrease in V_{th}. Thus, V_{th} was extracted by fitting these parameters. The extracted DOS values are specified in Tables 1 and 2, respectively, and $N_d = 2.7 \times 10^{17}$ (or 1.0×10^{17}) cm^{-3} for MoS_2 W/O

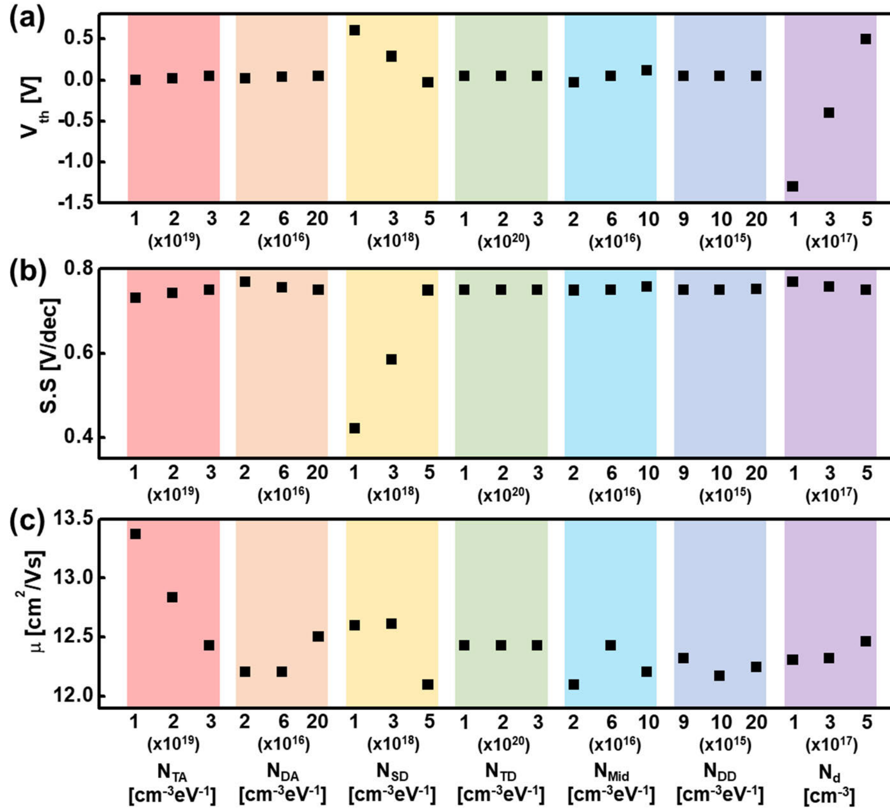

FIGURE 9. Plots of electrical parameters such as (a) V_{th}, (b) S.S, and (c) μ, corresponding to trap level variation.

TABLE 1. Summary of model parameters which are extracted from acceptor-like and donor-like states models to be fitted with subgap density of states (g(E)) for m-MoS_2 FETs without CYTOP passivation after PBS (or NBS), respectively. Initial stands for m-MoS_2 FETs without PBS (or NBS).

	DOSs W/O CYTOP	Initial	PBS	NBS
	N_{TA} [$eV^{-1}cm^{-3}$] / kT_{TA} [eV]	3×10^{19} / 0.02 (identical for initial, PBS, NBS)		
	N_{DA} [$eV^{-1}cm^{-3}$] / kT_{DA} [eV]	3×10^{16} / 0.2 (identical for initial, PBS, NBS)		
	N_{DD} [$eV^{-1}cm^{-3}$] / kT_{DD} [eV]	1.5×10^{16} / 0.85 (identical for initial, PBS, NBS)		
	N_{TD} [$eV^{-1}cm^{-3}$] / kT_{TD} [eV]	3×10^{20} / 0.03 (identical for initial, PBS, NBS)		
N_{Mid}	N_{Mid} [$eV^{-1}cm^{-3}$] / kT_{Mid} [eV] / E_{Mid} [eV]	1×10^{17} / 0.25 / 0.5	-	-
	$N_{HS2(+1)}$[$eV^{-1}cm^{-3}$] / $kT_{HS2(+1)}$[eV] / $E_{HS2(+1)}$[eV]	-	7×10^{16}/ 0.12 / 0.7	2.5×10^{16} / 0.11 / 0.78
	$N_{HS2(-1)}$ [$eV^{-1}cm^{-3}$] / $kT_{HS2(-1)}$[eV] / $E_{HS2(-1)}$ [eV]	-	1.5×10^{17}/ 0.05 / 0.37	2×10^{16} / 0.10 / 0.45
N_{SD}	N_{SD} [$eV^{-1}cm^{-3}$] / kT_{SD} [eV] / E_{SD} [eV]	3×10^{18}/ 0.06 / 0.17	-	-
	$N_{VS(0)}$ [$eV^{-1}cm^{-3}$] / $kT_{VS(0)}$ [eV] / $E_{VS(0)}$ [eV]	-	8×10^{17} / 0.08 / 0.18	4×10^{18} / 0.05 / 0.19
	$N_{VS(-1)}$ [$eV^{-1}cm^{-3}$] / $kT_{VS(-1)}$ [eV] / $E_{VS(-1)}$ [eV]	-	4×10^{18}/ 0.08 / 0.05	2×10^{18} / 0.05 / 0.08

(or W/) CYTOP. In addition, the actual physical dimension of W/L (= 30/10 μm) was used for this simulation study. Fig. 10 shows that the simulated I-V characteristics are compared with the experimental data obtained from the electrical measurement of the I–V characteristics for all bias stresses and encapsulation conditions. The transfer characteristics were measured at a fixed drain-to-source voltage (V_{DS}) of 0.1 V at room temperature. All results indicate that the transfer characteristics in the TCAD simulation are nicely matched with the measured transfer characteristics, substantiating that extracted subgap-DOSs information is physically meaningful.

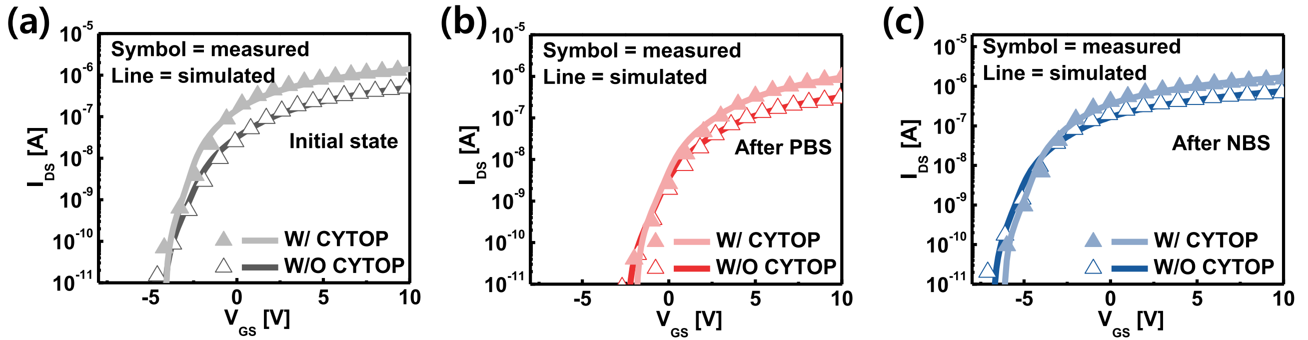

FIGURE 10. Measured (Symbol) and T-CAD model-based (Line) (a) initial transfer characteristics and transfer characteristics after (b) PBS and (c) NBS in m-MoS_2 FET without and with CYTOP encapsulation.

TABLE 2. Summary of model parameters which are extracted from acceptor-like and donor-like states models to be fitted with subgap density of states (g(E)) for m-MoS_2 FETs with CYTOP passivation after PBS (or NBS), respectively. Initial stands for m-MoS_2 FETs without PBS (or NBS).

	DOSs W/ CYTOP	Initial	PBS	NBS
	N_{TA} [$eV^{-1}cm^{-3}$] / kT_{TA} [eV]	2×10^{19} / 0.025 (identical for initial, PBS, NBS)		
	N_{DA} [$eV^{-1}cm^{-3}$] / kT_{DA} [eV]	2×10^{15} / 0.2 (identical for initial, PBS, NBS)		
	N_{DD} [$eV^{-1}cm^{-3}$] / kT_{DD} [eV]	9×10^{15} / 0.85 (identical for initial, PBS, NBS)		
	N_{TD} [$eV^{-1}cm^{-3}$] / kT_{TD} [eV]	1.5×10^{20} / 0.03 (identical for initial, PBS, NBS)		
N_{Mid}	N_{Mid} [$eV^{-1}cm^{-3}$] / kT_{Mid} [eV] / E_{Mid} [eV]	2×10^{16} / 0.2 / 0.52	-	-
	$N_{HS2(+1)}$[$eV^{-1}cm^{-3}$] / $kT_{HS2(+1)}$[eV] / $E_{HS2(+1)}$[eV]	-	2.5×10^{16} / 0.09 / 0.62	1×10^{16} / 0.15 / 0.76
	$N_{HS2(-1)}$ [$eV^{-1}cm^{-3}$] / $kT_{HS2(-1)}$[eV] / $E_{HS2(-1)}$ [eV]	-	1×10^{17}/ 0.04 / 0.37	9×10^{15} / 0.07 / 0.45
N_{SD}	N_{SD} [$eV^{-1}cm^{-3}$] / kT_{SD} [eV] / E_{SD} [eV]	1×10^{18} / 0.07 / 0.19	-	-
	$N_{VS(0)}$ [$eV^{-1}cm^{-3}$] / $kT_{VS(0)}$ [eV] / $E_{VS(0)}$ [eV]	-	6×10^{17} / 0.08 / 0.18	1.2×10^{18} / 0.06 / 0.21
	$N_{VS(-1)}$ [$eV^{-1}cm^{-3}$] / $kT_{VS(-1)}$ [eV] / $E_{VS(-1)}$ [eV]	-	1.5×10^{18} / 0.05 / 0.08	9×10^{17}/ 0.06 / 0.08

IV. CONCLUSION

For the future application of backplanes in flat panel displays, along with hybrid integration Si devices with 2-dimensional transition metal dichalcogenides, reliable device operation and its securing stable device configuration with optimization of 2D semiconductors and dielectrics are starting points for practical circuit-level applications. Thus, in this study, reliable and quantitative estimation of the bias stress instability of m-MoS_2 FETs for the respective PBS and NBS were systematically performed. To secure reliable m-MoS_2 FETs, the devices were encapsulated with CYTOP, leading to decoupling with external effects associated with ambient gas (e.g., O_2 and H_2O) in air. As one of the systematic methods for the extraction of subgap-DOSs, optical charge-pumping capacity-voltage spectroscopy was adopted, and hence, the extraction of DOSs and their evolution of DOSs for the respective PBS (or NBS) were investigated. With respect to the extracted DOSs at midgap and shallow trap levels, originating from V_S and V_{S2}, respectively, peak positions were shifted upward after PBS, leading to a state transition from V_S to V_S (-1) by electron trapping in the subgap states. Moreover, states of V_S (-1), which have a larger negative charge than that of V_S (0), transitioned toward V_S (0), and H_{S2} (0) was shifted toward H_{S2} $(+1)$, owing to the attraction of holes during NBS. In addition, compared with that of N_{Mid} for the initial state, the N_{Mid} peak with the highest value was changed from 0.50 eV to 0.37 eV (or 0.78 eV) after PBS (or NBS). Likewise, the N_{SD} peak was changed from the initial value of 0.17 eV to 0.05 eV (or 0.21 eV) after PBS (or NBS), accordingly. Variations in electrical parameters after bias stress rationally match the trend observed from DOSs information. Last, TCAD simulation substantiates that the extracted subgap DOSs information according to PBS (or NBS) is physically meaningful, leading to self-manifestation of the validity of the extracted DOSs information in I-V characteristics. Herein, the platform, which was secured for evaluation on subgap-DOSs for m-MoS_2 FETs, is expected to hint at the quantitative information behind the mechanism, which is closely related to device instabilities but hard to analyze due to previously reported methods associated active area limitation and unresolved information on both charge carriers and transport for each bias condition, relying on one-sided evaluation for either I-V or C-V characterization, respectively.

ACKNOWLEDGMENT

(Ga Won Yang, Seung Gi Seo, and Sungju Choi contributed equally to this work.)

REFERENCES

[1] K. Roy, S. Mukhopadhyay, and H. Mahmoodi-Meimand, "Leakage current mechanisms and leakage reduction techniques in deep-submicrometer CMOS circuits," *Proc. IEEE*, vol. 91, no. 2, pp. 305–327, Feb. 2003.

[2] Z. Abbas and M. Olivieri, "Impact of technology scaling on leakage power in nano-scale bulk CMOS digital standard cells," *Microelectron. J.*, vol. 45, no. 2, pp. 179–195, Feb. 2014.

[3] Q. H. Wang, K. Kalantar-Zadeh, A. Kis, J. N. Coleman, and M. S. Strano, "Electronics and optoelectronics of two-dimensional transition metal dichalcogenides," *Nature Nanotechnol.*, vol. 7, no. 11, pp. 699–712, Nov. 2012.

[4] D. Jariwala, V. K. Sangwan, L. J. Lauhon, T. J. Marks, and M. C. Hersam, "Emerging device applications for semiconducting two-dimensional transition metal dichalcogenides," *ACS Nano*, vol. 8, no. 2, pp. 1102–1120, Feb. 2014.

[5] X. Huang, Z. Zeng, and H. Zhang, "Metal dichalcogenide nanosheets: Preparation, properties and applications," *Chem. Soc. Rev.*, vol. 42, no. 5, pp. 1934–1946, 2013.

[6] M. Chhowalla, H. S. Shin, G. Eda, L.-J. Li, K. P. Loh, and H. Zhang, "The chemistry of two-dimensional layered transition metal dichalcogenide nanosheets," *Nature Chem.*, vol. 5, no. 4, pp. 263–275, Apr. 2013.

[7] Y. Y. Illarionov, A. J. Molina-Mendoza, M. Waltl, T. Knobloch, M. M. Furchi, T. Mueller, and T. Grasser, "Reliability of next-generation field-effect transistors with transition metal dichalcogenides," in *Proc. IEEE Int. Rel. Phys. Symp. (IRPS)*, Mar. 2018, p. 5A.

[8] W. H. Lee, H. H. Choi, D. H. Kim, and K. Cho, "25th anniversary article: Microstructure dependent bias stability of organic transistors," *Adv. Mater.*, vol. 26, no. 11, pp. 1660–1680, Mar. 2014.

[9] Y. P. Venkata Subbaiah, K. J. Saji, and A. Tiwari, "Atomically thin MoS_2: A versatile nongraphene 2D material," *Adv. Funct. Mater.*, vol. 26, no. 13, pp. 2046–2069, Apr. 2016.

[10] B. Radisavljevic, A. Radenovic, J. Brivio, V. Giacometti, and A. Kis, "Single-layer MoS_2 transistors," *Nat. Nanotechnol.*, vol. 6, no. 3, pp. 147–150, 2011.

[11] D. Jariwala, V. K. Sangwan, D. J. Late, J. E. Johns, V. P. Dravid, T. J. Marks, L. J. Lauhon, and M. C. Hersam, "Band-like transport in high mobility unencapsulated single-layer MoS_2 transistors," *Appl. Phys. Lett.*, vol. 102, no. 17, Apr. 2013, Art. no. 173107.

[12] G. He, K. Ghosh, U. Singisetti, H. Ramamoorthy, R. Somphonsane, G. Bohra, M. Matsunaga, A. Higuchi, N. Aoki, S. Najmaei, Y. Gong, X. Zhang, R. Vajtai, P. M. Ajayan, and J. P. Bird, "Conduction mechanisms in CVD-grown monolayer MoS_2 transistors: From variable-range hopping to velocity saturation," *Nano Lett.*, vol. 15, no. 8, pp. 5052–5058, Aug. 2015.

[13] H. Wang, L. Yu, Y.-H. Lee, Y. Shi, A. Hsu, M. L. Chin, L.-J. Li, M. Dubey, J. Kong, and T. Palacios, "Integrated circuits based on bilayer MoS_2 transistors," *Nano Lett.*, vol. 12, no. 9, pp. 4674–4680, Sep. 2012.

[14] M. Choi, Y. J. Park, B. K. Sharma, S. R. Bae, S. Y. Kim, and J. H. Ahn, "Flexible active-matrix organic light-emitting diode display enabled by MoS_2 thin-film transistor," *Sci. Adv.*, vol. 4, no. 4, 2018, Art. no. eaas8721.

[15] R. Kumar, P. K. Kulriya, M. Mishra, F. Singh, G. Gupta, and M. Kumar, "Highly selective and reversible NO_2 gas sensor using vertically aligned MoS_2 flake networks," *Nanotechnology*, vol. 29, no. 46, 2018, Art. no. 464001.

[16] S. Zandi, P. Saxena, M. Razaghi, and N. E. Gorji, "Simulation of CZTSSe thin-film solar cells in COMSOL: Three-dimensional optical, electrical, and thermal models," *IEEE J. Photovolt.*, vol. 10, no. 5, pp. 1503–1507, Sep. 2020.

[17] Y. Chen, G. Gao, J. Zhao, H. Zhang, J. Yu, X. Yang, Q. Zhang, W. Zhang, S. Xu, J. Sun, Y. Meng, and Q. Sun, "Piezotronic graphene artificial sensory synapse," *Adv. Funct. Mater.*, vol. 29, no. 41, Oct. 2019, Art. no. 1900959.

[18] X. Yang, J. Han, J. Yu, Y. Chen, H. Zhang, M. Ding, C. Jia, J. Sun, Q. Sun, and Z. L. Wang, "Versatile triboiontronic transistor via proton conductor," *ACS Nano*, vol. 14, no. 7, pp. 8668–8677, Jul. 2020.

[19] X. Yang, J. Yu, J. Zhao, Y. Chen, G. Gao, Y. Wang, Q. Sun, and Z. L. Wang, "Mechanoplastic tribotronic floating-gate neuromorphic transistor," *Adv. Funct. Mater.*, vol. 30, no. 34, 2020, Art. no. 2002506.

[20] A. Rai, H. C. P. Movva, A. Roy, D. Taneja, S. Chowdhury, and S. K. Banerjee, "Progress in contact, doping and mobility engineering of MoS_2: An atomically thin 2D semiconductor," *Crystals*, vol. 8, no. 8. p. 316, 2018.

[21] S. Das, H.-Y. Chen, A. V. Penumatcha, and J. Appenzeller, "High performance multilayer MoS_2 transistors with scandium contacts," *Nano Lett.*, vol. 13, no. 1, pp. 100–105, Jan. 2013.

[22] K. K. H. Smithe, C. D. English, S. V. Suryavanshi, and E. Pop, "Intrinsic electrical transport and performance projections of synthetic monolayer MoS_2 devices," *2D Mater.*, vol. 4, no. 1, 2017, Art. no. 011009.

[23] S. M. Gali, A. Pershin, A. Lherbier, J.-C. Charlier, and D. Beljonne, "Electronic and transport properties in defective MoS_2: Impact of sulfur vacancies," *J. Phys. Chem. C*, vol. 124, no. 28, pp. 15076–15084, Jul. 2020.

[24] H. Yuan, H. Shen, J. Li, J. Shao, D. Huang, Y. Chen, P. F. Wang, S. J. Ding, A. Chin, and M. Li, "PBTI investigation of MoS_2 n-MOSFET with Al_2O_3 gate dielectric," *IEEE Electron Device Lett.*, vol. 38, no. 5, pp. 677–680, May 2017.

[25] Y. Y. Illarionov, G. Rzepa, M. Waltl, T. Knobloch, A. Grill, M. M. Furchi, T. Mueller, and T. Grasser, "The role of charge trapping in MoS_2/SiO_2 and MoS_2/hBN field-effect transistors," *2D Mater.*, vol. 3, no. 3, 2016, Art. no. 035004.

[26] Y. Y. Illarionov, T. Knobloch, M. Waltl, G. Rzepa, A. Pospischil, D. K. Polyushkin, M. M. Furchi, T. Mueller, and T. Grasser, "Energetic mapping of oxide traps in MoS_2 field-effect transistors," *2D Mater.*, vol. 4, no. 2, 2017, Art. no. 025108.

[27] Y. Y. Illarionov, K. K. H. Smithe, M. Waltl, T. Knobloch, E. Pop, and T. Grasser, "Improved hysteresis and reliability of MoS_2 transistors with high-quality CVD growth and Al_2O_3 encapsulation," *IEEE Electron Device Lett.*, vol. 38, no. 12, pp. 1763–1766, Dec. 2017.

[28] S. Choi, S. G. Seo, H. R. Yu, S. Y. Kim, D. H. Kim, and S. H. Jin, "Hydrophobic polymer encapsulation effects on subgap density of states in multilayered molybdenum disulfide field-effect transistors," *Phys. Status Solidi (RRL)–Rapid Res. Lett.*, vol. 14, no. 1, 2019, Art. no. 1900492.

[29] M. Takenaka, Y. Ozawa, J. Han, and S. Takagi, "Quantitative evaluation of energy distribution of interface trap density at MoS_2 MOS interfaces by the terman method," in *IEDM Tech. Dig.*, Dec. 2016, p. 5.

[30] H. Bae, C. K. Kim, and Y. K. Choi, "Characterization of intrinsic subgap density-of-states in exfoliated MoS_2 FETs using a multi-frequency capacitance-conductance technique," *AIP Adv.*, vol. 7, no. 7, 2017, Art. no. 075304.

[31] Q. Xu, Y. Sun, P. Yang, and Y. Dan, "Density of defect states retrieved from the hysteretic gate transfer characteristics of monolayer MoS_2 field effect transistors," *AIP Adv.*, vol. 9, no. 1, Jan. 2019, Art. no. 015230.

[32] K. Cho, W. Park, J. Park, H. Jeong, J. Jang, T.-Y. Kim, W.-K. Hong, S. Hong, and T. Lee, "Electric stress-induced threshold voltage instability of multilayer MoS_2 field effect transistors," *ACS Nano*, vol. 7, no. 9, pp. 7751–7758, Sep. 2013.

[33] S. Yang, S. Park, S. Jang, H. Kim, and J.-Y. Kwon, "Electrical stability of multilayer MoS_2 field-effect transistor under negative bias stress at various temperatures," *Phys. Status Solidi (RRL)–Rapid Res. Lett.*, vol. 8, no. 8, pp. 714–718, Aug. 2014.

[34] H. Qiu, L. Pan, Z. Yao, J. Li, Y. Shi, and X. Wang, "Electrical characterization of back-gated bi-layer MoS_2 field-effect transistors and the effect of ambient on their performances," *Appl. Phys. Lett.*, vol. 100, no. 12, 2012, Art. no. 123104.

[35] W. Park, J. Park, J. Jang, H. Lee, H. Jeong, K. Cho, S. Hong, and T. Lee, "Oxygen environmental and passivation effects on molybdenum disulfide field effect transistors," *Nanotechnology*, vol. 24, no. 9, Mar. 2013, Art. no. 095202.

[36] H.-J. Kwon, J. Jang, S. Kim, V. Subramanian, and C. P. Grigoropoulos, "Electrical characteristics of multilayer MoS_2 transistors at real operating temperatures with different ambient conditions," *Appl. Phys. Lett.*, vol. 105, no. 15, Oct. 2014, Art. no. 152105.

[37] J. Roh, I.-T. Cho, H. Shin, G. Woo Baek, B. Hee Hong, J.-H. Lee, S. Hun Jin, and C. Lee, "Fluorinated CYTOP passivation effects on the electrical reliability of multilayer MoS_2 field-effect transistors," *Nanotechnology*, vol. 26, no. 45, Nov. 2015, Art. no. 455201.

[38] K. Jeon, C. Kim, I. Song, J. Park, S. Kim, S. Kim, Y. Park, J.-H. Park, S. Lee, D. M. Kim, and D. H. Kim, "Modeling of amorphous InGaZnO thin-film transistors based on the density of states extracted from the optical response of capacitance-voltage characteristics," *Appl. Phys. Lett.*, vol. 93, no. 18, Nov. 2008, Art. no. 182102.

[39] H. Bae, H. Choi, S. Jun, C. Jo, Y. H. Kim, J. S. Hwang, J. Ahn, S. Oh, J.-U. Bae, S.-J. Choi, D. H. Kim, and D. M. Kim, "Single-scan monochromatic photonic capacitance-voltage technique for extraction of subgap DOS over the bandgap in amorphous semiconductor TFTs," *IEEE Electron Device Lett.*, vol. 34, no. 12, pp. 1524–1526, Dec. 2013.

[40] Y. G. Mo, M. Kim, and H. D. Kim, "Amorphous-oxide TFT backplane for large-sized AMOLED TVs," *J. Soc. Inf. Display*, vol. 19, no. , pp. 16–20, 2011.

[41] H. H. Hsieh, T. Kamiya, K. Nomura, H. Hosono, and C. C. Wu, "Modeling of amorphous $InGaZnO_4$ thin film transistors and their subgap density of states," *Appl. Phys. Lett.*, vol. 92, no. 13, pp. 10–13, 2008.

[42] E. Fortunato, P. Barquinha, and R. Martins, "Oxide semiconductor thin-film transistors: A review of recent advances," *Adv. Mater.*, vol. 24, no. 22, pp. 2945–2986, Jun. 2012.

[43] K. Nomura, H. Ohta, A. Takagi, T. Kamiya, M. Hirano, and H. Hosono, "Room-temperature fabrication of transparent flexible thin-film transistors using amorphous oxide semiconductors," *Nature*, vol. 432, no. 7016, pp. 488–492, Nov. 2004.

[44] S. G. Seo and S. H. Jin, "Bias temperature stress instability of multilayered MoS_2 field-effect transistors with CYTOP passivation," *IEEE Trans. Electron Devices*, vol. 66, no. 5, pp. 2208–2213, May 2019.

[45] S. G. Seo, J. Joeng, K. Kim, K. Kim, and S. H. Jin, "Bias stress instability in multilayered MoS_2 field-effect transistors under pulse-mode operation," *IEEE Trans. Electron Devices*, vol. 67, no. 4, pp. 1864–1872, Apr. 2020.

[46] S. Kc, R. C. Longo, R. Addou, R. M. Wallace, and K. Cho, "Impact of intrinsic atomic defects on the electronic structure of MoS_2 monolayers," *Nanotechnology*, vol. 25, no. 37, 2014, Art. no. 375703.

[47] J. Yang, H. Kawai, C. P. Y. Wong, and K. E. J. Goh, "Electrical doping effect of vacancies on monolayer MoS_2," *J. Phys. Chem. C*, vol. 123, no. 5, pp. 2933–2939, Feb. 2019.

[48] B. Zhao, C. Shang, N. Qi, Z. Y. Chen, and Z. Q. Chen, "Stability of defects in monolayer MoS_2 and their interaction with O_2 molecule: A first-principles study," *Appl. Surf. Sci.*, vol. 412, pp. 385–393, Aug. 2017.

[49] K. Choi, S. R. A. Raza, H. S. Lee, P. J. Jeon, A. Pezeshki, S.-W. Min, J. S. Kim, W. Yoon, S.-Y. Ju, K. Lee, and S. Im, "Trap density probing on top-gate MoS_2 nanosheet field-effect transistors by photo-excited charge collection spectroscopy," *Nanoscale*, vol. 7, no. 13, pp. 5617–5623, 2015.

[50] S. G. Seo, J. H. Hong, J. H. Ryu, and S. H. Jin, "Low-frequency noise characteristics in multilayer $MoTe_2$ FETs with hydrophobic amorphous fluoropolymers," *IEEE Electron Device Lett.*, vol. 40, no. 2, pp. 251–254, Feb. 2019.

[51] S.-C. Lu and J.-P. Leburton, "Electronic structures of defects and magnetic impurities in MoS_2 monolayers," *Nanosc. Res. Lett.*, vol. 9, no. 1, p. 676, Dec. 2014.

[52] A. Singh and A. K. Singh, "Origin of N-type conductivity of monolayer MoS_2," *Phys. Rev. B, Condens. Matter*, vol. 99, no. 12, Mar. 2019, Art. no. 121201.

[53] H. P. Komsa and A. V. Krasheninnikov, "Native defects in bulk and monolayer MoS_2 from first principles," *Phys. Rev. B, Condens. Matter*, vol. 91, no. 12, 2015, Art. no. 125304.

[54] S. H. Song, M. K. Joo, M. Neumann, H. Kim, and Y. H. Lee, "Probing defect dynamics in monolayer MoS_2 via noise nanospectroscopy," *Nature Commun.*, vol. 8, no. 1, p. 2121, 2017.

[55] D. L. Tiwari and K. Sivasankaran, "Impact of carrier concentration and bandgap on the performance of double gate GNR-FET," *Superlattices Microstruct.*, vol. 130, pp. 38–49, Jun. 2019.

[56] D. L. Tiwari and K. Sivasankaran, "Nitrogen-doped NDR behavior of double gate graphene field effect transistor," *Superlattices Microstruct.*, vol. 136, Dec. 2019, Art. no. 106308.

[57] D. L. Tiwari and K. Sivasankaran, "NDR behavior of a phosphorous-doped double-gate MoS_2 armchair nanoribbon field effect transistor," *J. Electron. Mater.*, vol. 49, no. 1, pp. 551–558, Jan. 2020.

GA WON YANG received the B.S. degree in electrical engineering from Kookmin University, Seoul, South Korea, in 2020, where she is currently pursuing the M.S. degree with the Department of Electrical Engineering.

SEUNG GI SEO received the B.S. and M.S. degrees in electronic engineering from Incheon National University, Incheon, South Korea, in 2018 and 2020, respectively, where he is currently pursuing the Ph.D. degree in electronic engineering.

SUNGJU CHOI received the B.S., M.S., and Ph.D. degrees in electrical engineering from Kookmin University, Seoul, South Korea, in 2014, 2016 and 2021, respectively.

DAE HWAN KIM (Senior Member, IEEE) received the B.S., M.S., and Ph.D. degrees in electrical engineering from Seoul National University, Seoul, South Korea, in 1996, 1998, and 2002, respectively.

He is currently a Professor with the School of Electrical Engineering, Kookmin University, Seoul. His current research interests include nano CMOS, oxide and organic thin film transistors, biosensors, and neuromorphic devices.

SUNG HUN JIN received the M.S. and Ph.D. degrees in electrical engineering from Seoul National University (SNU), Seoul, South Korea, in 2000 and 2006, respectively.

He is currently an Associate Professor with the Department of Electronic Engineering, Incheon National University. His current research interests include low dimensional materials (1D, 2D) based devices and circuits for flexible electronics.